Aalborg Universitet

AALBORG UNIVERSITY
DENMARK

Quantitative Assessment Mechanism of Low Frequency Oscillations in Train-Network Systems

Kong, Rui; Sahoo, Subham; Lyu, Xiaoqin; Wang, Xiaoru; Blaabjerg, Frede

Published in:
Sustainable Energy, Grids and Networks

Publication date:
2024

Link to publication from Aalborg University

Citation for published version (APA):
Kong, R., Sahoo, S., Lyu, X., Wang, X., & Blaabjerg, F. (2024). Quantitative Assessment Mechanism of Low Frequency Oscillations in Train-Network Systems. *Sustainable Energy, Grids and Networks*.

General rights
Copyright and moral rights for the publications made accessible in the public portal are retained by the authors and/or other copyright owners and it is a condition of accessing publications that users recognise and abide by the legal requirements associated with these rights.

- Users may download and print one copy of any publication from the public portal for the purpose of private study or research.
- You may not further distribute the material or use it for any profit-making activity or commercial gain
- You may freely distribute the URL identifying the publication in the public portal -

Take down policy
If you believe that this document breaches copyright please contact us at vbn@aub.aau.dk providing details, and we will remove access to the work immediately and investigate your claim.

Quantitative Assessment Mechanism of Low Frequency Oscillations in Train-Network Systems

Rui Kong[a], Subham Sahoo[a], Xiaoqin Lyu[b], Xiaoru Wang[b], Frede Blaabjerg[a]

[a]*Department of Energy, Aalborg University, Aalborg, 9220, Denmark*
[b]*School of Electrical Engineering, Southwest Jiaotong University, Chengdu, 610031, China*

Abstract

Low frequency oscillations (LFOs) in the electrified train-network system can lead to serious traction blockade accidents. Although impedance models and stability analysis tools have been applied in existing studies to address specific cases, a generalized mechanism to address LFO is still not established so far. This paper proposes a quantitative assessment method to reveal the underlying mechanism of LFOs. Founded on the improved Nyquist criterion, a stability margin indicator is defined to concretely describe system stability, then its corresponding expression is derived by combining the simplified impedance model as the basis for quantitative analysis. To this end, the identified negative resistances in the impedance model are revealed as the root cause of LFOs. Besides, theoretical justification for the impact of parameter tuning on the system stability is provided based on the explicit formula of the stability margin indicator. Finally, the effectiveness and accuracy of the theoretical analysis are verified under simulations and hardware-in-the-loop experimental conditions.

Keywords: train-network system, low frequency oscillation, mechanism analysis, quantitative assessment

1. Introduction

With the widespread evolution of electric trains, traction converter dynamics may cause harmonic instability across a wide frequency range [1, 2, 3], in which low frequency oscillations (LFOs) usually occur when multiple trains are energized in a rail depot under the low-power operation mode [4, 5, 6, 7].

LFOs are characterized by continuous voltage and current oscillations below 10 Hz, which causes serious negative effects on the traction transformer, and even traffic interruption due to protection system action[7].

For the LFO issues in the train-network system, the impedance analysis method has been widely applied due to its high computational efficiency, modularity, and scalability [8, 9]. The multiple-input-multiple-output (MIMO)small-signal impedance models of the train-network system in the d-q frame were established in [4, 7, 10, 11]. On this basis, the dominant pole analysis is used to identify system damping [4], and the forbidden region-based criterion with less conservatism is proposed to assess system stability [10]. Further, the generalized Nyquist criterion is utilized to depict the system stability threshold and influence factors more precisely in [12, 13]. However, these criteria can only judge the stability of the train-network system without quantifying the respective contributions of the traction network and the electric train to the LFO for mechanism analysis. In order to thoroughly understand the LFO phenomenon and provide a solid theoretical foundation for LFO mitigation in the future, it is necessary to reveal the underlying causes and key influence factors of LFOs.

On the one hand, to find the root cause of LFOs, the RLC circuit model of train-network system is modeled in [14, 15], which found that LFOs can be regarded as a consequence of low frequency resonance between an inductive traction network and capacitive trains with negative resistance characteristics. By analyzing the Bode diagram of the impedance model, [11] shows that there is a negative resistance in the d-d channel impedance of the train converter, but cannot identify the source of negative resistance due to a large number of matrix calculations in the impedance modeling. By drawing analogous research results of other grid-connected converters, it is found that the frequency-coupling mechanism of switching modulation and sampling process can lead to negative resistance in the range of high frequency [16, 17]. However, it cannot be used to formalize the explanation behind LFOs in the low frequency range. Moreover, the phase-locked loop (PLL) of the three-phase grid-tied inverters can bring negative resistance in the low frequency range [18, 19], yet it is not applicable in train-network systems, since the PLL dynamics only have a slight impact on the traction converter's impedance under low-power rectifier operation mode [20]. Therefore, LFO traceability in train-network systems still needs further research.

On the other hand, since the system stability is jointly determined by the parameters of the train and network, one theory arises that LFO occurs

due to the parameter mismatch between the traction network and the train converter [2],[10], and parameter tuning is a low-cost yet effective oscillation suppression measure [21, 22]. In light of this, the questions of interest are which parameters have a significant impact on the LFO, and whether the tunning of these parameters will have a positive or negative effect on the system. The case studies in [10, 13, 14, 15, 23] demonstrate that the key system parameters affect system stability significantly. Nevertheless, the case-based analysis using existing criteria can only draw empirical conclusions by observing the change in the stability criteria after adjusting a certain parameter and summarizing the results of multiple case studies, where the confidence in results needs to be verified by extensive experiments or statistical analysis. Therefore, the essential influence mechanism of the parameters is still unclear due to the lack of exact expressions that can quantitatively describe the relationship between system stability and parameters.

To fill these gaps, a quantitative assessment method is developed for the stability analysis of the train-network system in this paper, aiming at revealing the formation mechanism of LFOs and the impact mechanism of model parameters with explicit mathematical expressions, providing a solid theoretical basis for LFO mitigation. The main contributions of this paper are as follows:

1. By decomposing the conventional Nyquist criterion into frequency response curves, a key stability margin indicator is defined. The significant feature and attraction of this stability margin indicator is that its explicit mathematical expression can be derived as the basis of the in-depth quantitative LFO mechanism analysis.
2. Based on the simplified d-q impedance model of the train converter, the root cause of LFO is clarified by deriving the stability margin indicator.
3. The relationship between key parameters and the system stability margin indicator is derived, and a theoretical justification of the impact of parameter tuning on system stability is revealed.

The rest of this paper is organized as follows. Section 2 describes the studied train-network system and the conventional LFO analysis method based on the generalized Nyquist criterion with some defects. In Section 3, the quantitative mechanism assessment method is formulated to reveal the LFO mechanism based on the defined stability margin indicator. Section 4 shows the case studies with simulation results and experimental verification. Section 5 gives the conclusions.

2. Problem Formulation

2.1. System Description

The system diagram of train-network system and train traction drive units is shown in Fig. 1, where each train consists of multiple parallel traction drive units with the same structure and powered by onboard transformers. It is worth mentioning that the LFO most often occurs when multiple trains are energized in the same rail depot with only auxiliary loads, such as lighting [7], and the traction inverters & motors remain standstill. Hence, the DC-side of the traction drive unit can be equivalenced to a constant-value large resistance R_d [6, 7, 10, 11], with our focus completely on the grid-side converters. In addition, the distance between trains parking at the same depot is very close, which avoids the need to consider the impedance of the connecting lines between different trains [24]. On the other hand, the traction network is equivalent to a series circuit of inductance L_s and resistance R_s [4], since the effect of distributed capacitance in the traction network is negligible in the low-frequency range.

Due to fast dynamic response and simple implementation, the transient direct current control (TDCC) strategy is widely used in electric train converters [3, 21, 25]. In the TDCC strategy as shown in Fig. 2, the phase θ tracked by phase-locked loop (PLL) is used to generate the sine and cosine signals, which are combined with the output signal of DC-Link voltage controller (DVC) i_n^{ref} to compose the reference input signal of the current controller (CC) $i_n^{ref}\sin\theta$ and compensation signal $\omega L_n i_n^{ref}\cos\theta$, $R_n i_n^{ref}\sin\theta$. It should be noted that only a proportional controller is used in CC because of its AC input. The DVC's output signal i_n^{ref} includes an effective component i_n^f to improve the dynamic response of the PI controller. Moreover, the grid-side voltage signal u_n as the input signal of the CC needs to be filtered by band-pass filter (BPF), and the second-order generalized integrator (SOGI) is essentially a BPF, which can also output u_α^* and u_β^* with a phase difference of 90° as the input signal of the PLL. Actually, SOGI-PLL is a proven integral control structure applied widely for single-phase grid-connected converters due to its fast dynamics, good accuracy, and high immunity to harmonic distortions [26]. The main circuit and control parameters of the train-network system are listed in Table I.

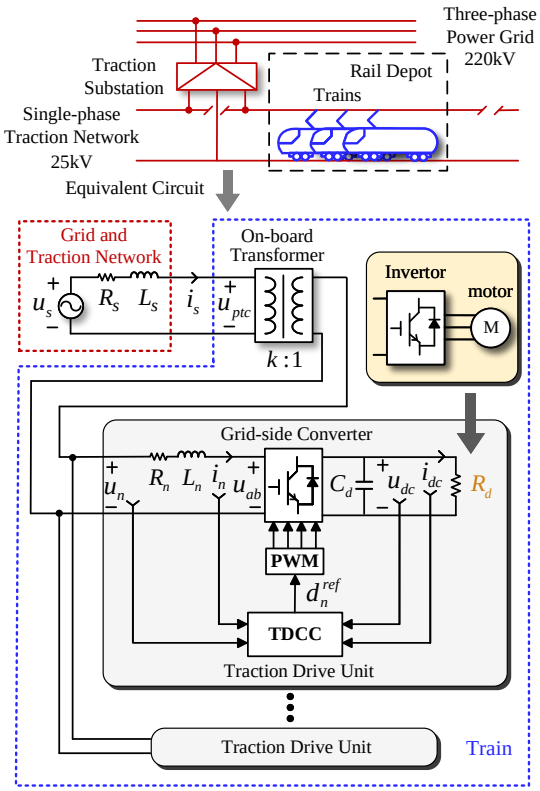

Figure 1: System diagram of train-network system and train traction drive units.

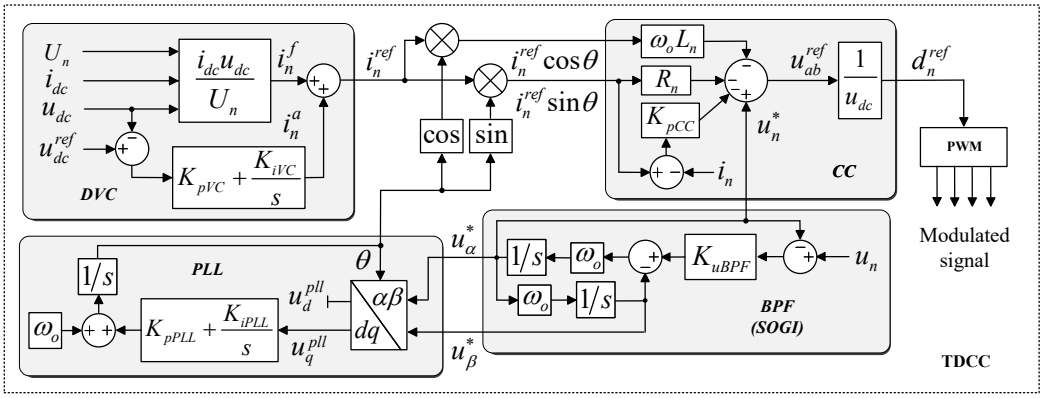

Figure 2: Control diagram of train converters – Transient direct current control (TDCC).

Table 1: Parameters of Train-Network System

Symbol / Unit	**Description**	**Parameters**
U_n/V	AC voltage effective value of converter	1550
I_n/A	AC current effective value of converter	5.8
U_{dc}/V	DC link referencevoltage of converter	3000
R_n/Ω	Equivalent resistance of onboard transformer	0.15
L_n/mH	Equivalent inductance of onboard transformer	4
R_d/Ω	DC link Load resistance	1000
C_d/mF	DC link support capacitance	9
f_s/Hz	Switching frequency	350
T_d/ms	Time delay of PWM	0.15
K_{BPF}	Proportional gain of BPF	0.5
K_{pPLL}	Proportional gain of PLL	0.7
K_{iPLL}	Integral gain of PLL	25
K_{pVC}	Proportional gain of DVC	0.28
K_{iVC}	Integral gain of DVC	20
K_{pCC}	Proportional gain of CC	0.2
R_S/Ω	Equivalent resistance of traction network	0.2
L_S/mH	Equivalent inductance of traction network	24

2.2. Conventional Impedance-Based Stability Analysis Method

According to the impedance modeling theory, the train-network system in Fig. 1 can be regarded as a cascaded system as shown in Fig. 3, where $\mathbf{Z}_S$ is the grid-side impedance, which can be expressed in dq-frame as [4]:

$$\mathbf{Z}_S = \begin{bmatrix} R_s + sL_s & -\omega_o L_s \\ \omega_o L_s & R_s + sL_s \end{bmatrix} \tag{1}$$

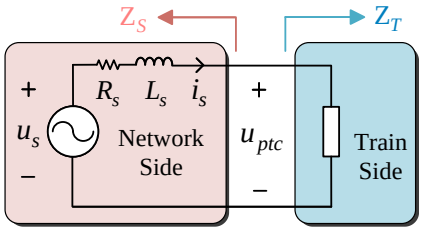

Figure 3: Equivalent cascaded impedance model of train-network system – Input impedance of train converters and output impedance of traction network.

Moreover, $\mathbf{Z}_T$ is the train-side impedance to the primary side of the on-board transformer, which can be expressed as:

$$\mathbf{Z}_T = (k^2 \mathbf{Z}_C)/pm \tag{2}$$

where, k is the on-board transformer ratio and p is the number of converters in a train, m is the number of trains energized in the same rail depot, and $\mathbf{Z}_C$ is the linearized impedance model of the train converter under TDCC in dq-frame. The modelling process of $\mathbf{Z}_C$ have been elaborated in [27], to give:

$$\mathbf{Z}_C = (\mathbf{M}_{IU} + \mathbf{M}_{ID}\mathbf{M}_1\mathbf{M}_3)^{-1}(\mathbf{I} - \mathbf{M}_{ID}\mathbf{M}_1\mathbf{M}_2) \tag{3}$$

where, $\mathbf{I}$ is the second-order identity matrix, and $\mathbf{M}_1$, $\mathbf{M}_2$, $\mathbf{M}_3$ can be respectively expressed as:

$$\begin{cases} \mathbf{M}_1 = [\mathbf{I} + \mathbf{M}_{DEL}(\mathbf{M}_{CC} - \mathbf{M}_{COM})\mathbf{M}_{DVC}\mathbf{M}_{DCD} + \mathbf{M}_{DEL}\mathbf{M}_{DC}\mathbf{M}_{DCD}]^{-1} \\ \mathbf{M}_2 = \mathbf{M}_{DEL}\left[\mathbf{M}_{CC} - (\mathbf{M}_{CC} - \mathbf{M}_{COM})\mathbf{M}_{DVC}\mathbf{M}_{DCI} - \mathbf{M}_{DC}\mathbf{M}_{DCI}\right] \\ \mathbf{M}_3 = \mathbf{M}_{DEL}\mathbf{M}_{EP}\mathbf{M}_{BPF} \end{cases}$$

The expressions of each matrix in (3) are shown in Appendix A. After establishing the grid-side impedance model $\mathbf{Z}_S$ and train-side impedance model

$\mathbf{Z}_T$ respectively, the open-loop impedance ratio matrix $\mathbf{L}_K$ is obtained as:

$$\mathbf{L}_K = \mathbf{Z}_S(\mathbf{Z}_T)^{-1} = \frac{pm}{k^2}\frac{\mathbf{Z}_S}{\mathbf{Z}_C} \tag{4}$$

Both the traction network and train are stable respectively with reasonable parameter settings, meaning that the number of poles of $\mathbf{L}_K$ in the right half complex plane is zero [4]. According to the generalized Nyquist criterion (GNC) [12], if the Nyquist curves corresponding to the two eigenvalues of $\mathbf{L}_K$, i.e., λ_{k1} and λ_{k2}, do not enclose the (-1+j0) point, the system is stable, otherwise, the system is unstable.

2.3. Disadvantages of Case-Based Analysis Method

According to GNC, the influence of parameters on the system stability can be summarized by observing whether the Nyquist curves encircle the point (-1+j0) and the changing trend of the Nyquist curve after adjusting the parameters. This kind of case-specific method has been widely applied in past studies [10, 13, 14, 15, 23]. Repeated experiments with a large number of cases can improve the reliability of these conclusions, but case-based analysis still lacks solid theoretical support.

In addition, optimizing controllers or adjusting system parameters are effective LFO mitigation solutions, which need to be implemented based on thoroughly clarified LFO mechanisms and key influencing factors. However, the case-based method cannot provide reliable information for the design of LFO mitigation options. Therefore, it is necessary to reveal the root cause of LFOs and the clear relationship between parameters and system stability.

3. Proposed Quantitative Mechanism Assessment Method

To make up for the disadvantages of case-specific approaches, a quantitative mechanism assessment method is proposed in this paper. To be specific, the GNC is improved to define the stability margin indicator, whose exact expression is derived by combining the simplified impedance model, which can quantitatively reveal the essential reasons for the risk of LFO and the impact of parameter tuning on the system stability. A comparison between the conventional impedance method and the proposed quantitative assessment method is shown in Fig. 4.

3.1. Definition of Stability Margin Indicator

By adding the impedance ratio matrix $\mathbf{L}_K$ and the second-order identity matrix $\mathbf{I}$, the matrix $\mathbf{L}_R$ can be obtained as:

$$\mathbf{L}_R = \mathbf{I} + \mathbf{L}_K \tag{5}$$

According to the eigenvalue formula of the second-order matrix, the relationship between the eigenvalues of $\mathbf{L}_K$, namely λ_{k1} and λ_{k2}, and the eigenvalues of $\mathbf{L}_R$, namely λ_{r1} and λ_{r2}, can be expressed as:

$$\begin{cases} \mathrm{Re}[\lambda_{r1}] = 1 + \mathrm{Re}[\lambda_{k1}] \\ \mathrm{Re}[\lambda_{r2}] = 1 + \mathrm{Re}[\lambda_{k2}] \\ \mathrm{Im}[\lambda_{r1}] = \mathrm{Im}[\lambda_{k1}] \\ \mathrm{Im}[\lambda_{r2}] = \mathrm{Im}[\lambda_{k2}] \end{cases} \tag{6}$$

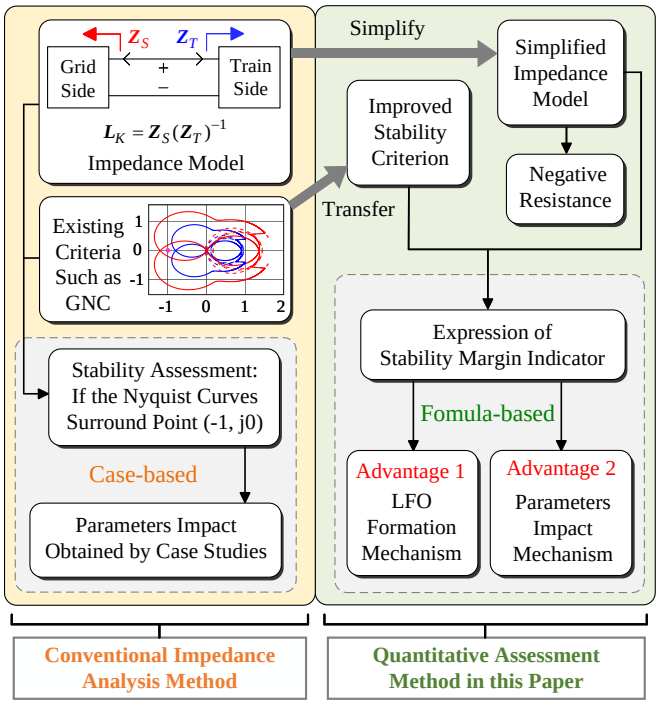

Figure 4: Comparison between the conventional impedance analysis method and the proposed quantitative assessment method (GNC: generalized Nyquist criterion, LFO: Low frequency oscillation).

Nyquist curves are the trajectories of the real and imaginary parts of the matrix eigenvalues varying with the frequency. Hence, as compared to the original Nyquist curve of λ_{k1} and λ_{k2}, the Nyquist curves of λ_{r1} and λ_{r2} will shift by one unit to the right along the real axis. As a result, the stability assessment criterion based on $\mathbf{L}_R$ should be expressed as, if the Nyquist curves of λ_{r1} and λ_{r2} do not encircle the point (0, j0) in s-plane, the system will be stable, otherwise it will be unstable. Although there are two eigenvalues of $\mathbf{L}_R$, one of them is more likely to surround the (0, j0) point and play a dominant role in determining the system stability, which is called the dominant eigenvalue, denoted as λ_m.

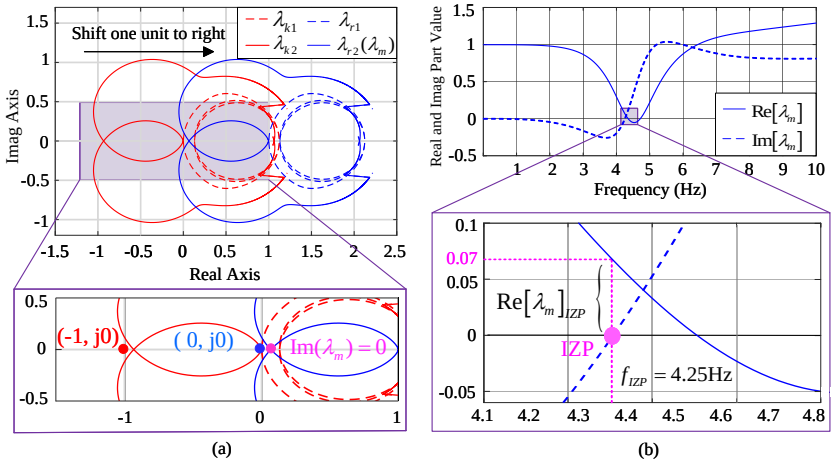

Figure 5: Frequency response curves (b) evolved from Nyquist curves (a) – Definition of stability margin indicator $\mathrm{Re}\,[\lambda_m]_{IZP}$ (IZP: zero-crossing point).

Nyquist curves varying with frequency can be decomposed into the frequency response curves of the real parts and imaginary parts of the eigenvalues. Fig. 5(a) demonstrates the shifting and decomposing process, where λ_m is λ_{r2} in this case. Fig. 5(b) plots the frequency response curves of $\mathrm{Re}\,[\lambda_m]$ and $\mathrm{Im}\,[\lambda_m]$, where only the vital low frequency range between 0-10 Hz are highlighted to show the analysis results more clearly. As shown in Fig. 5(a), the imaginary part of λ_m is zero at the leftmost intersection of the Nyquist curve of λ_m with the real axis. This intersection corresponds to the imaginary part zero-crossing point (IZP) in Fig. 5(b), where f_{IZP} is the frequency corresponding to IZP, and $\mathrm{Re}\,[\lambda_m]_{IZP}$ is the real part of λ_m when $f = f_{IZP}$.

As a result, the positive value of $\mathrm{Re}\,[\lambda_m]_{IZP}$ corresponds to the Nyquist

curve of λ_m not encircling the point (0, j0), so the system is stable. On the contrary, if $\mathrm{Re}\,[\lambda_m]_{IZP}$ is negative, the system will be unstable. Therefore, $\mathrm{Re}\,[\lambda_m]_{IZP}$ is defined as the stability margin indicator since its positive or negative value can reflect whether the system is stable or not.

3.2. Simplified Impedance Model and Analytical Eigenvalues

3.2.1. Model simplification

In order to obtain the explicit expression of stability margin indicator $\mathrm{Re}\,[\lambda_m]_{IZP}$, establishing the simplified impedance model of train converter is necessary, which avoids complicated matrix calculations. Except for the basic PI controller in the voltage-current double loop, the effect of other control components on the system impedance model is compared as shown in Fig. 6. It can be seen that before and after ignoring the PLL or i_n^f component in the DVC, the amplitude and phase curves of the impedance model are almost unchanged, and thus they can be disregarded. However, if the compensation of CC is neglected, the magnitude and phase of the d-d and q-d channels of the impedance model will deviate significantly from the original complete impedance model in the low-frequency range (1-10 Hz), indicating its non-negligible importance.

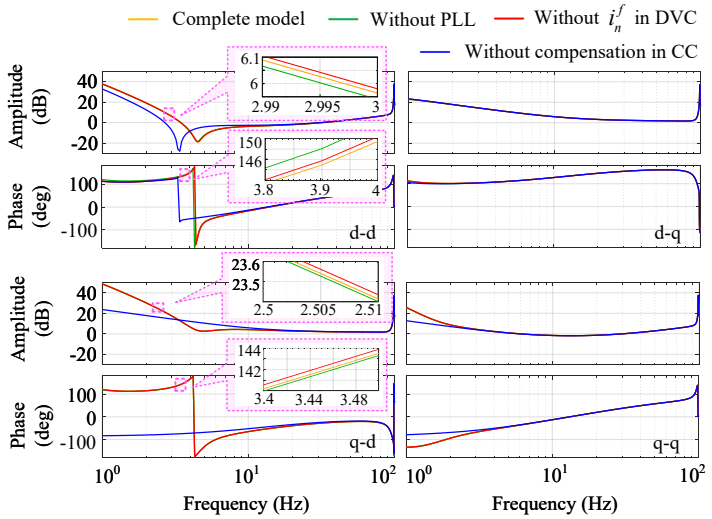

Figure 6: Bode plots of converter impedance model after neglecting different control components

Moreover, in the LFO scenario, DC side equivalent resistance R_d is much

larger than the equivalent inductance of onboard transformer R_n. By combining this point with the expression of the variable steady-state value in Appendix A, the simplified main circuit model can be obtained. On this basis, considering the conclusions drawn from Fig. 6, the following equations can be obtained from the converter impedance model in (3) and matrix expressions in Appendix A.

$$\begin{aligned} \Delta i_d^{ref} &= -(K_{pVC} + \frac{K_{iVC}}{s})\Delta u_{dc} \\ &= -(K_{pVC} + \frac{K_{iVC}}{s})\frac{0.5U_d}{sC_dU_{dc}}\Delta i_d \end{aligned} \tag{7}$$

$$\begin{aligned} \begin{bmatrix} \Delta u_d \\ \Delta u_q \end{bmatrix} &= \begin{bmatrix} sL_n + R_n & -\omega_o L_n \\ \omega_o L_n & sL_n + R_n \end{bmatrix} \begin{bmatrix} \Delta i_d \\ \Delta i_q \end{bmatrix} \\ &- G_d K_{pCC} \begin{bmatrix} \Delta i_d^{ref} - \Delta i_d & 0 \\ 0 & \Delta i_q^{ref} - \Delta i_q \end{bmatrix} + G_d \begin{bmatrix} \Delta u_d - R_n \Delta i_d^{ref} \\ \Delta u_q - \omega_o L_n \Delta i_d^{ref} \end{bmatrix} \end{aligned} \tag{8}$$

where, $[\Delta x_d, \Delta x_q]^T$ represent the small-signal space vectors of corresponding variables in the d-q frame ($x = u_n, i_n, i_n^{ref}$ in the single-phase stationary frame). G_d is the first-order inertial link equivalent to PWM. Moreover, $G_d = 1 \,/\, (1 + sT_d)$, and T_d is the delay time caused by PWM [7].

By substituting (7) into (8), the simplified impedance model of the TDCC converter $\mathbf{Z}_{CS}$ can be obtained, where the Laplace operator is set as $s = j\omega$, and the higher-order terms above the second order can be neglected since they will be fast attenuation with increasing frequency. Finally, each element of $\mathbf{Z}_{CS}$ can be expressed respectively as:

$$\begin{cases} Z_{dd}^{cs} = R_n + \dfrac{L_n}{T_d} - \dfrac{K_{pVC}(K_{pCC}+R_n)U_d}{2T_d\omega^2 C_d U_{dc}} + j(\omega L_n - \dfrac{R_n + K_{pCC}}{T_d\omega}) \\ Z_{dq}^{cs} = -\omega_o L_n + j\dfrac{\omega_o L_n}{T_d\omega} \\ Z_{qd}^{cs} = \omega_o L_n - \dfrac{K_{pVC}(\omega_o L_n)U_d}{2T_d\omega^2 C_d U_{dc}} - j\dfrac{\omega_o L_n}{T_d\omega} \\ Z_{qq}^{cs} = R_n + \dfrac{L_n}{T_d} + j(\omega L_n - \dfrac{R_n + K_{pCC}}{T_d\omega}) \end{cases} \tag{9}$$

where ω_o is the fundamental rotational angular frequency, and $\omega = 2\pi f$.

3.2.2. Negative resistance

The expressions of each element of the simplified impedance matrix in (9) indicate that there are negative resistances brought by DVC in the d-d and q-d channels, which can be expressed as:

$$\begin{cases} R_{dd}^{n} = -K_{pVC}(K_{pCC}+R_n)\dfrac{0.5U_d}{T_d\omega^2 C_d U_{dc}} \\ R_{qd}^{n} = -K_{pVC}(\omega_o L_n)\dfrac{0.5U_d}{T_d\omega^2 C_d U_{dc}} \end{cases} \tag{10}$$

It can be seen in (10) that the negative resistances attenuate as the frequency increases, so they mainly affect the impedance in the low frequency range. Moreover, based on (7) and (10), it can be found that the negative resistances are introduced by Δi_d^{ref}. As a result, the reason for the existence of negative resistance in the impedance model of the train's converter can be explained by analyzing the influence path of the DVC's output signal i_n^{ref}, namely i_d^{ref} in dq-frame. In the structure diagram of TDCC as shown in Fig. 2, i_n^{ref} is not only input to the proportional controller of the CC as $-K_{pCC}(i_n^{ref} - i_n)$, but also constitutes the compensation signal of the CC as $R_n i_n^{ref}\sin\theta$ and $\omega L_n i_n^{ref}\cos\theta$. They are denoted as $-K_{pCC}(\Delta i_d^{ref} - \Delta i_d)$ and $-R_n\Delta i_d^{ref}$ in the d-d channel and $-\omega_o L_n \Delta i_d^{ref}$ in the q-d channel during the impedance modeling process in the d-q frame, which can be clearly seen in (8). Therefore, there are two corresponding formation paths of the negative resistances, by which negative resistances are brought to the d-d and q-d

channel of the impedance model as shown in Fig. 7.

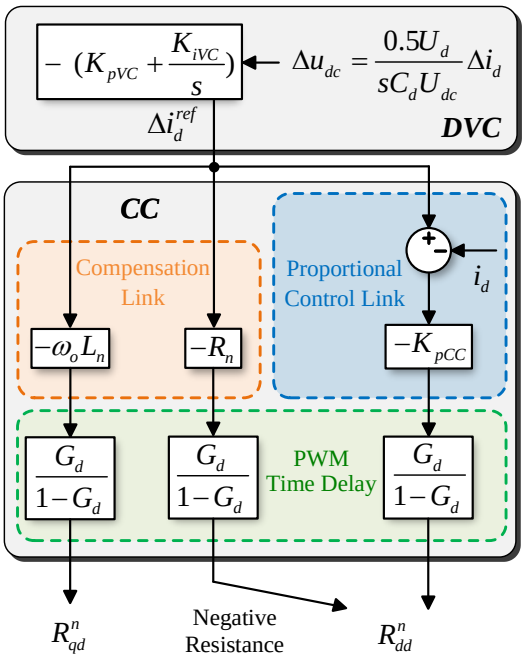

Figure 7: Formation paths of negative resistances – Negative resistances are brought by DVC and affected by CC.

3.2.3. Analytical eigenvalues

After replacing the detailed impedance model $\mathbf{Z}_C$ in (4) with simplified impedance model $\mathbf{Z}_{CS}$, the impedance ratio matrix $\mathbf{L}_K$ in the d-q frame is transformed linearly to obtain the matrix $\mathbf{L}_K^{seq}$ in the modified sequence domain [28]. $\mathbf{L}_K^{seq}$ has the same eigenvalues as $\mathbf{L}_K$, and it is a diagonally dominant matrix whose non-diagonal elements can be neglected [24]. Hence, $\mathbf{L}_K^{seq}$ can be expressed as:

$$\begin{aligned}\mathbf{L}_K^{seq} &= \mathbf{A}_Z\mathbf{L}_K\mathbf{A}_Z^{-1} = n\mathbf{A}_Z\mathbf{Z}_S\mathbf{A}_Z^{-1}[\mathbf{A}_Z(\mathbf{Z}_T)\mathbf{A}_Z^{-1}]^{-1} \\ &= \frac{mp}{(k)^2}\begin{bmatrix} Z_{pp}^s / Z_{pp}^{cs} & 0 \\ 0 & Z_{nn}^s / Z_{nn}^{cs} \end{bmatrix}\end{aligned} \tag{11}$$

where,

$$
\begin{cases}
Z_{pp}^{s} = R_s + j\omega L_s + j\omega_o L_s \\
Z_{nn}^{s} = R_s + j\omega L_s - j\omega_o L_s \\
Z_{pp}^{cs} = R_n + \dfrac{L_n}{T_d} + \dfrac{\omega_o L_n}{T_d\omega} + \dfrac{1}{2}R_{dd}^{n} + j[(\omega+\omega_o)L_n - \dfrac{R_n + K_{pCC}}{T_d\omega} + \dfrac{1}{2}R_{qd}^{n}] \\
\quad \triangleq Z_{R+} + \dfrac{1}{2}R_{dd}^{n} + j(Z_{I+} + \dfrac{1}{2}R_{qd}^{n}) \\
Z_{nn}^{cs} = R_n + \dfrac{L_n}{T_d} - \dfrac{\omega_o L_n}{T_d\omega} + \dfrac{1}{2}R_{dd}^{n} + j[(\omega-\omega_o)L_n - \dfrac{R_n + K_{pCC}}{T_d\omega} - \dfrac{1}{2}R_{qd}^{n}] \\
\quad \triangleq Z_{R-} + \dfrac{1}{2}R_{dd}^{n} + j(Z_{I-} - \dfrac{1}{2}R_{qd}^{n})
\end{cases}
$$

The diagonal elements in (11) can be regarded as the eigenvalues of $\mathbf{L}_K^{seq}$ and $\mathbf{L}_K$. Furthermore, the eigenvalues of $\mathbf{L}_R$ are obtained according to (6) as:

$$
\begin{cases}
\lambda_{r1} = 1 + \dfrac{mp}{(k)^2}\dfrac{Z_{pp}^{s}}{Z_{pp}^{cs}} \\
\lambda_{r2} = 1 + \dfrac{mp}{(k)^2}\dfrac{Z_{nn}^{s}}{Z_{nn}^{cs}}
\end{cases}
\tag{12}
$$

By substituting Z_{pp}^{s}, Z_{nn}^{s}, Z_{pp}^{cs}, Z_{nn}^{cs} of (11) into (12), the real part and imaginary part of the eigenvalues in (12) can be obtained, which are not given in detail here for brevity considering their complex expressions.

3.3. Formation Mechanism Analysis of LFO

According to the definition of the system stability margin indicator in Section 3.1, the expression of $\mathrm{Re}\,[\lambda_m]_{IZP}$ can be obtained by capturing the real part of λ_m when the imaginary part of λ_m is zero. Since the dominant eigenvalue λ_m is one of the two eigenvalues in (12) depending on the specific system situation, in order to avoid redundant elaboration, λ_{r2} is taken as λ_m for detailed derivation. Hence, let $\mathrm{Im}[\lambda_m]$ be zero, (13) can be obtained as:

$$
Z_{I-} = \frac{(\omega_{IZP} - \omega_o)(Z_{R-} + \dfrac{1}{2}R_{dd})L_s}{R_s} + \frac{R_{qd}}{2} \tag{13}
$$

The frequency at IZP named ω_{IZP} can be obtained according to (13), and then ω_{IZP} is substituted into $\mathrm{Re}[\lambda_m]$ to derive the explicit expression of

$\mathrm{Re}\,[\lambda_m]_{IZP}$, which can be finally given by:

$$\mathrm{Re}[\lambda_m]_{IZP} = \mathrm{Re}[\lambda_{r2}]_{IZP} = 1 + \mathrm{Re}[\lambda_{k2}]_{IZP} = 1 + \frac{mp}{(k)^2}\frac{(\omega_o - \omega_{IZP})L_s}{-Z_{I-} + 0.5R_{qd}^n} \quad (14)$$

When ω_{IZP} is in the low frequency range, $\omega_o - \omega_{IZP} > 0$. In addition, the inequality $Z_{I-} < 0$ holds when the parameters are within the normal range: the orders of magnitude of R_n, L_n and T_d are between 10^{-4} and 10^{-2}, while the orders of magnitude of K_{pVC} and K_{pCC} are generally between 10^{-1} and 10^{1}. As a result, if negative resistance R_{qd}^n caused by DVC is neglected, $\mathrm{Re}[\lambda_{k2}]_{IZP}$ must be positive, and there must be $\mathrm{Re}[\lambda_m]_{IZP} > 1$ in the low frequency range, indicating that the system must be stable. However, the existence of R_{qd}^n makes it possible for $\mathrm{Re}[\lambda_{k2}]_{IZP}$ to be negative, resulting in the risk of LFO. Therefore, the negative resistance caused by DVC is the root reason for LFO. The above analysis process is shown in Fig. 8.

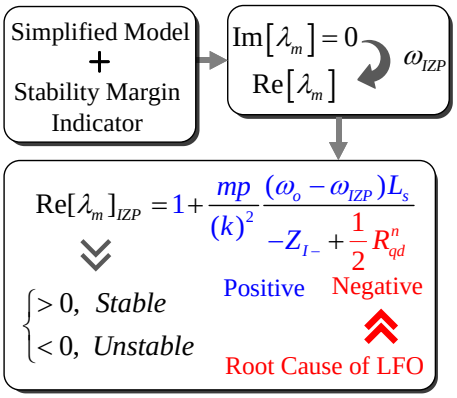

Figure 8: Analysis process of the formation mechanism of LFO – Negative resistance is the root cause of LFO.

3.4. Quantitative Assessment of Parameters Impact on LFO

Based on the explicit expression of $\mathrm{Re}[\lambda_m]_{IZP}$ in (14), the factors contributing to systemic instability risks and the impact of the parameters on the system stability can also be quantitatively demonstrated, which is different from conventional case-specific analysis. It is worth noting that $\mathrm{Re}\,[\lambda_m]_{IZP}$ is not only determined by $\mathrm{Re}\,[\lambda_m]$, but also related to ω_{IZP}, and ω_{IZP} is independent of $\mathrm{Re}\,[\lambda_m]$. As shown in Fig. 9, the impact of a certain parameter X

on the system stability indicator $\mathrm{Re}\,[\lambda_m]_{IZP}$ (Magenta) can be decomposed into its impact on $\mathrm{Re}\,[\lambda_m]$ (Red) and ω_{IZP} (Blue) for analysis, respectively.

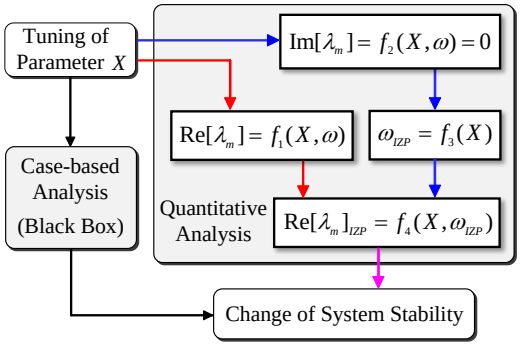

Figure 9: Impact mechanism of parameters on system stability – Parameters impacts on $Re\,[\lambda_m]$ and ω_{IZP} work together.

The parameters of train-network system include traction network-side parameters and train-side parameters. On the one hand, a weak grid network tends to cause the instability of grid-connected converters, and it can be seen from (14) that the increase in the impedance of the traction network (i.e., weaker grid network) can be equivalent to the increase in the number of trains. On the other hand, for train-side parameters, the control parameters are more feasible to adjust compared to the determined circuit parameters of the train. Therefore, the number and control parameters of trains will be used as examples to analyze the impact of parameters on LFO through the proposed assessment method.

3.4.1. Impact of the number of trains

According to Fig. 9, when analyzing the impact of the number of trains m on the system stability, it is necessary to consider its impact on ω_{IZP} and $\mathrm{Re}[\lambda_m]$ at the same time. As for ω_{IZP}, it can be found by setting $\mathrm{Im}[\lambda_m]$ to zero, and m can be neglected in this process because it is just a coefficient exerting no influence on the result as shown in (15).

$$\mathrm{Im}[\lambda_m] = \mathrm{Im}[\lambda_{r2}] = \frac{mp}{(k)^2}\frac{(\omega-\omega_o)L_s(Z_{R-}+\frac{1}{2}R^n_{dd}) - R_s(Z_{I-}-\frac{1}{2}R^n_{qd})}{(Z_{R-}+\frac{1}{2}R^n_{dd})^2 + (Z_{I-}-\frac{1}{2}R^n_{qd})^2} \quad (15)$$

However, (14) shows the negative resistance may make $\mathrm{Re}[\lambda_{k2}]_{IZP}$ nega-

tive. At the same time, when the number of trains m increases, the negative $\mathrm{Re}[\lambda_{k2}]_{IZP}$ will be smaller, i.e., the impact of negative resistance is amplified. As a result, When m increases to a certain value such that $\mathrm{Re}[\lambda_{k2}]_{IZP}$ is less than -1, $\mathrm{Re}[\lambda_m]_{IZP}$ will be negative, thereby leading to LFOs in the system.

3.4.2. Impact of the key control parameters

It has been known that the negative resistance brought by DVC is the root cause of LFO, and the proportional gain of DVC denoted as K_{pVC} is included in the negative resistance as shown in (10), so K_{pVC} is the key parameter affecting the system stability.

Associating (13) with the definition of Z_{I-} in (11) when $\mathrm{Im}[\lambda_m]$ is zero (i.e., $\omega = \omega_{IZP}$), the expression of K_{pVC} can be derived. Then, by computing the partial derivative of K_{pVC} with respect to ω_{IZP}, the relationship between K_{pVC} and ω_{IZP} are obtained as:

$$\begin{aligned}\frac{\partial K_{pVC}}{\partial \omega_{IZP}} = &\frac{[(2\omega_{IZP}A - B)(2\omega_{IZP} - \omega_o) + C](D - E\omega_o)}{[E(\omega_{IZP} + \omega_o) - D]^2} \\ &+ \frac{[(2\omega_{IZP}A - B)E - AD]{\omega_{IZP}}^2}{[E(\omega_{IZP} + \omega_o) - D]^2}\end{aligned} \tag{16}$$

where,

$$\begin{cases} A = R_n + \dfrac{L_n}{T_d} - \dfrac{L_n}{L_s}R_s,\ B = \dfrac{\omega_o L_n}{T_d} \\ C = \dfrac{(R_n + K_{pCC})R_s}{L_s T_d},\ D = \dfrac{R_s \omega_o L_n}{L_s}\dfrac{U_d}{4T_d C_d U_{dc}} \\ E = (K_{pCC} + R_n)\dfrac{U_d}{4T_d C_d U_{dc}} \end{cases}$$

It can be found that A, B, C, D and E are necessarily positive when parameters are within the normal range, i.e., the orders of magnitude of R_n, L_n and T_d are between 10^{-4} and 10^{-2}, while the orders of magnitude of K_{pVC} and K_{pCC} are generally between 10^{-1} and 10^{1}. On this basis, when ω_{IZP} is in the low frequency range, $2\omega_{IZP} - \omega_o < 0$, $2\omega_{IZP}A - B < 0$ and $D - E\omega_o < 0$ are always true. Therefore, it can be deduced from (16) that $\partial K_{pVC}/\partial \omega_{IZP} < 0$, indicating K_{pVC} is negatively correlated with ω_{IZP}.

Moreover, when the system is at the risk of instability, the negative resistance plays a leading role, and $|Z_{I-}|$ is much less than $\left|R_{qd}^n / 2\right|$ in (14),

which can be neglected. Therefore, by combining (10) and (14), the stability margin indicator is obtained approximatively as:

$$\mathrm{Re}[\lambda_m]_{IZP} = 1 + \mathrm{Re}[\lambda_{k2}]_{IZP} = 1 - \frac{mp}{(k)^2}\frac{4T_d C_d U_{dc} L_s(\omega_o - \omega_{IZP})\omega_{IZP}^2}{\omega_o L_n U_d K_{pVC}} \quad (17)$$

According to (16) and (17), when K_{pVC} increases, ω_{IZP} decreases, leading to a decrease of the absolute value of $\mathrm{Re}[\lambda_{k2}]_{IZP}$. Since $\mathrm{Re}[\lambda_{k2}]_{IZP}$ is negative itself, $\mathrm{Re}[\lambda_m]_{IZP}$ increases eventually, indicating that the system stability enhances as K_{pVC} increases.

The impact of other system parameters on LFO can be analyzed based on the similar process. Among them, the proportional gain of CC denoted as K_{pCC} is also a key control parameter. The detailed analysis for the impact of K_{pCC} will not be repeated here for brevity, and the analysis results are directly given. K_{pCC} is positively correlated with ω_{IZP}, so the increase of K_{pCC} causes ω_{IZP} increasing, which is negative for stability. However, the real part of the dominant eigenvalue increases, making $[\lambda_m]_{IZP}$ increase finally, i.e. system stability enhances as K_{pCC} increases.

To conclude, the parameter tuning can affect the system stability by affecting the real part of the dominant eigenvalue and the frequency at IZP together. As compared to the conventional case-specific analysis, the quantitative assessment method proposed in this section has a reliable theoretical foundation, which can explain the underlying reasons behind the impact of parameters on system stability.

3.4.3. Parameter Sensitivity Analysis

The sensitivity analysis of key parameters can be implemented based on the proposed stability margin indicator, which may be valuable to the system parameter optimization. The sensitivity of a specific parameter can be obtained by calculating the percentage of change in the stability margin indicator when this parameter is changed by 100% [15], which can be expressed as:

$$\delta = \left|\frac{(\vartheta^c - \vartheta^o)/\vartheta^o}{(\tau^c - \tau^o)/\tau^o}\right| \times 100\% \quad (18)$$

Where δ is the sensitivity of a parameter, τ^o and τ^c are the original/changed values of this parameter, ϑ^o and ϑ^c are the corresponding original/changed values of the stability margin indicator respectively.

4. Results and Verifications

4.1. Case Studies and Simulations

4.1.1. Verification of LFO formation mechanism

The Bode diagram of the impedance model of the converter before and after neglecting the DVC is provided in Fig. 10, where the impedance measurement results using frequency sweep method [11] based on simulation model are also shown. The original impedance model is highly consistent with the impedance measurement, and there are negative resistances in the d-d and q-d channels of impedance model with phase exceeding ±90° [23]. However, after neglecting the DVC, a significant difference can be seen in the low frequency range (< 10 Hz), showing the DVC brings negative impedance.

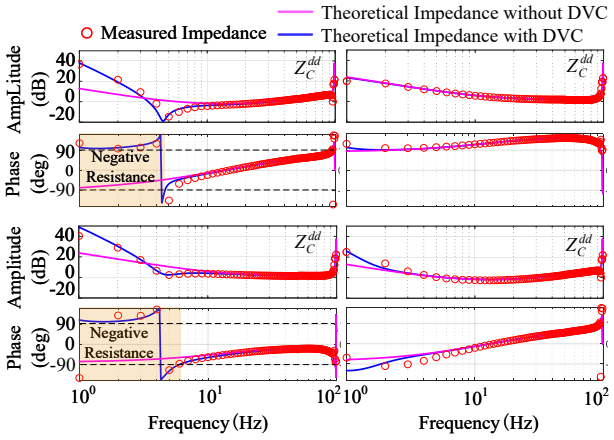

Figure 10: Bode plots of theoretical impedance with/without DVC and impedance measurement results – Negative resistances are brought by DVC at the low frequency range.

In order to illustrate the negative resistance brought by DVC is the root cause of LFO, a comparative result is given as shown in Fig. 11. When the number of trains is 8 and the DVC is considered, λ_{r2} has an IZP in the low frequency range, and $\mathrm{Re}\left[\lambda_{r2}\right]_{IZP}$ is negative, indicating that λ_{r2} is the dominant eigenvalue λ_m, and the system is unstable. However, when the DVC is neglected, there is no IZP of λ_{r2}, and $\mathrm{Re}\left[\lambda_{r2}\right]$ is always positive, indicating system becomes stable.

4.1.2. Verification of parameter impact

As shown in Fig. 12(a), with the increase of trains number m, the IZP of the dominant eigenvalue in the low frequency range does not change, whose

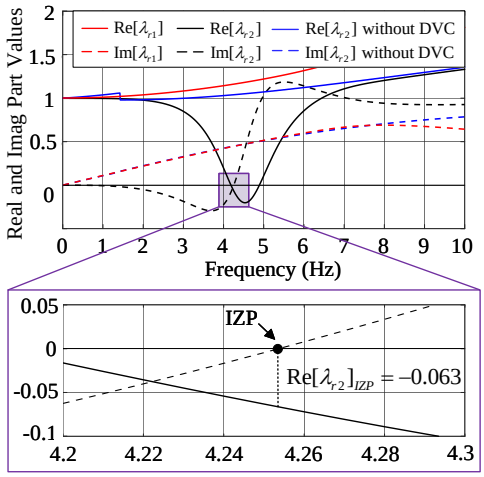

Figure 11: Stability analysis of train-network system with/without DVC – DVC is the root cause of LFO.

frequency is always 4.25 Hz, but the value of $\mathrm{Re}\,[\lambda_m]$ gradually decreases. When m is 6, there is $\mathrm{Re}\,[\lambda_m]_{IZP} = 0.468$, but When m increases to 8, there is $\mathrm{Re}\,[\lambda_m]_{IZP} = -0.063 < 0$, indicating the system is unstable. Combining the above results and (18), the sensitivity of train number m can be calculated as 113.46 %.

The corresponding time-domain simulation results are performed on Matlab/Simulink platform, which can be intuitively judged whether the LFO occurs by observing the waveforms of the voltage at the point of train connection u_{ptc}, current of traction network i_s and the DC-side voltage of the converter u_{dc}. Moreover, to quantitatively describe the oscillation waveforms, the ESPRIT algorithm [29] is used for the AC-side voltage signal to identify the oscillation frequency f_{LFO} and damping ratio coefficient σ. A positive/negative value of σ indicates the oscillation attenuation/amplitude, and the larger the absolute value of σ, the greater the oscillation change.

As shown in Fig. 12(b), as m increases from 6 to 8, the system waveform tends to oscillate, and the identified σ decreases from $11.9e^{-3}$ to -$1.7e^{-4}$. When $m = 8$, continuous LFO occurs at around 4.3 Hz. Therefore, the case analysis and simulation results match the analysis in Section 3.4.1.

As shown in Fig. 13(a), when the number of trains is 8 and K_{pVC} increases from 0.28 to 0.32, f_{IZP} decreases from 4.254 Hz to 4.216 Hz, while $\mathrm{Re}[\lambda_m]_{IZP}$ increases from -0.063 to 0.083, indicating that the system stability increases with the increase of K_{pVC}. Based on the above results and (18),

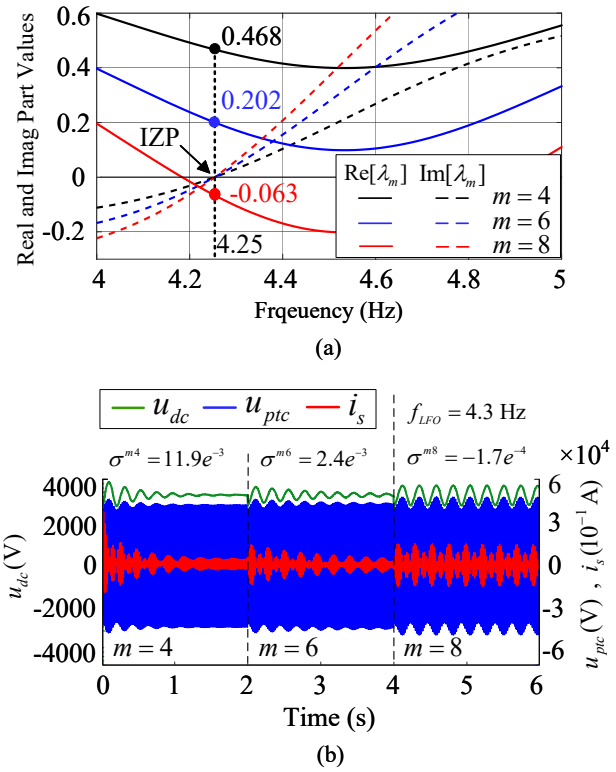

Figure 12: The impact of the number of trains on the system stability (a) model-based analysis results (b) simulation waveforms – Increase of the number of trains will weaken system stability without affecting the frequency at IZP.

the sensitivity of K_{pVC} can be calculated as 1622.22 %.

It can be seen from the corresponding simulation waveforms in Fig. 13(b) that, when K_{pVC} is 0.28, continuous LFO at around 4.3 Hz occurs and the identified σ is -1.7e^{-4}; but when K_{pVC} increases to 0.32, LFO is suppressed while σ increases to 2.7e^{-3}. The case analysis and simulation results comply with the theoretical quantitative assessment in Section 3.4.2.

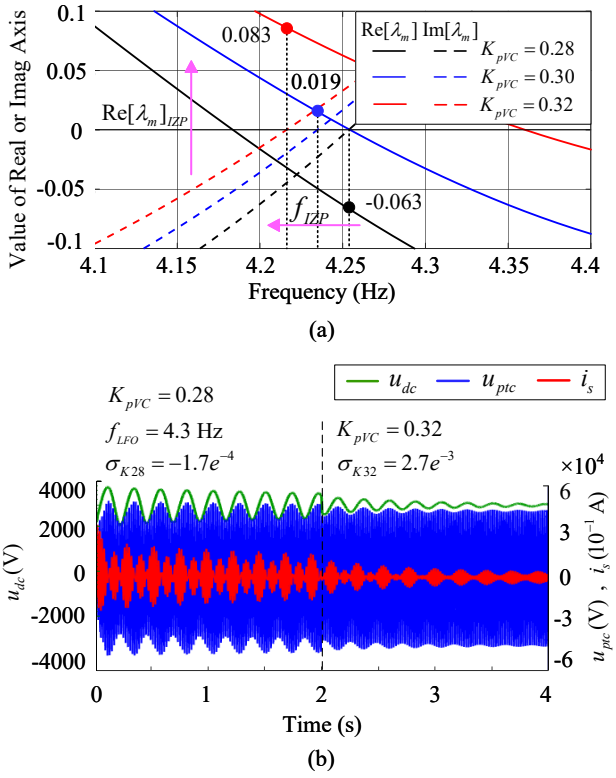

Figure 13: The impact of K_{pVC} on the system stability (a) model-based analysis results (b) simulation waveforms – Increase of proportional gain of DVC can decrease ω_{IZP} and increase Re[λ_m]$_{IZP}$, resulting in a final system stability enhancement.

In this section, the impact mechanism analysis of train number (m) and the proportional gain of DVC (K_{pVC}) are verified by case studies. Moreover, although both reducing m and increasing K_{pVC} can mitigate LFOs, the sensitivity analysis results show that the stability margin indicator is more significantly affected by K_{pVC}, so a small adjustment of K_{pVC} can achieve large stability improvement.

4.2. Experimental Verification

4.2.1. Experimental setup

Hardware-in-the-loop (HIL) real-time verification is carried out based on the Starsim experimental platform as shown in Fig. 14, which includes a host computer, a real-time simulator (NI-PXIe-FPGA-7868R), a real-time controller (NI-PXIe-FPGA-7846R), signal transmission ports (I/O boards), and an oscilloscope. The main circuit of the train-network system as shown in Fig. 1 is operated in the real-time simulator, and the control strategy with the same topology as shown in Fig. 2 is performed in the real-time controller, with the same parameters as listed in Table I. The real-time simulator converts the simulated analog signals to the range of $-10V \sim 10V$ and transfers them to the I/O boards. The analog signals are sampled by the internal ADC module in the real-time controller with a sampling frequency of 20 kHz. The calculated PWM pulses are then sent to the real-time simulator to control the train converter. The whole system can be controlled by StarSim software on the host computer.

In the experiment, the AC side voltage/current and DC side voltage are sampled to show the results of system stability. The sampling duration is 10 seconds and the parameter jump was set at 5th second.

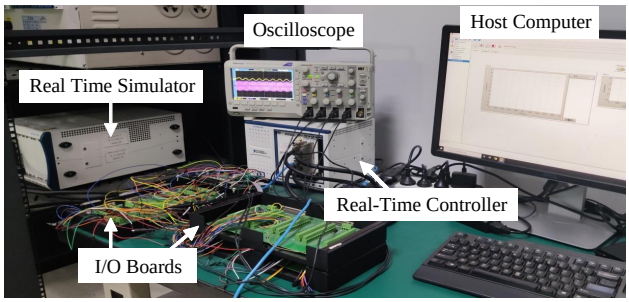

Figure 14: Starsim/HIL experiment platform of the system as shown in Fig. 1.

4.2.2. Experimental results

First, the theoretical derivation results point out that DVC is the root cause of LFO. Since control cannot be achieved correctly without using DVC, it is difficult to directly verify the impact of DVC through experimental comparison, but it can be achieved based on mathematical models, which has been demonstrated in Fig. 10 and Fig. 11. Fortunately, we can indirectly

prove the important role of DVC on LFO by observing the impact of K_{pVC} in the follow-up.

As for the impact of key parameters, when the number of trains m increases from 6 to 8, the experimental waveforms are shown in Fig. 15. It can be seen that when m is 6, the waveform tends to be mitigated, indicating that the stability margin indicator is positive and the train-network system is small-signal stable. But when m reaches 8, the stability margin indicator decreases according to the revealed influence mechanism, and it can be seen from Fig. 15 that sustained LFO occurs indicating that the stability margin indicator becomes negative. Therefore, the experiment result matches the simulation waveforms in Fig. 12 and establishes that the increase in the number of trains can weaken the stability of the train-network system in the low frequency range.

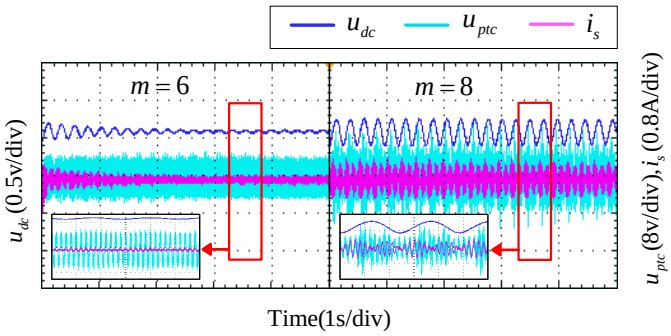

Figure 15: Experimental waveform of LFO – Increase of trains number m weakens the system stability.

As shown in Fig. 16, when the number of trains is 8 and the proportional gain of DVC (K_{pVC}) is 0.28, the experimental waveforms of the train-network system appear as the sustained LFO, indicating that the stability margin indicator is negative now. However, as K_{pVC} increases to 0.32, the stability margin indicator will increase according to the revealed influence mechanism, and thus the LFO gradually decays, meaning the stability margin increases to a positive value. The above experimental result is consistent with the simulation waveforms in Fig. 13, and it verifies that the increase of K_{pVC} can significantly enhance the system stability in the low frequency range.

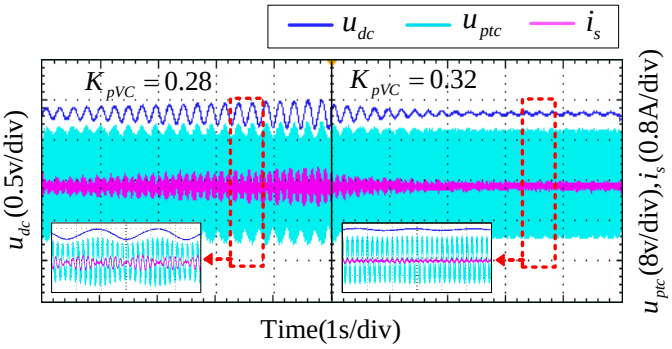

Figure 16: Experimental waveform of LFO – Increase of proportional gain of DVC K_{pVC} enhances the system stability.

5. Discussion

5.1. Advantages of the Proposed Analysis Method

Compared with existing case-based analysis methods, the proposed quantitative mechanism assessment method derives a specific mathematical expression of the stability margin indicator that can reflect the stability of the system for the first time. It is useful to clearly reveal the root cause of LFOs and further deduce the relationship between key parameters and system stability, mathematically explaining the influence mechanism of key parameters. Therefore, reliable analysis results can be obtained without verification by a large number of case studies, while providing a solid theoretical basis for LFO mitigation measures based on controller improvement or parameter adjustment.

5.2. Recommendations for Guidance

First, a stiff grid network is beneficial to prevent LFOs and accommodate a larger number of electric trains. Correspondingly, the situation of multiple trains stopping at the same location should be avoided or at least the number of stopping trains should be reduced. However, this may be limited by the realities of transportation demand and scheduling. By employing reactive power compensation, the traction substation capacity can be increased, but the cost of realizing this method is higher due to the expensive external devices [24]. In comparison, the control optimization approach is the easiest and low-cost option.

For the LFO mitigation in train-network systems with electric trains using TDCC control, parameter tuning guidance can be given according to the discussions in Section 3.4.2 that increasing the proportional gain of DVC and the proportional gain of CC can increase the stability margin indicator to mitigate LFOs. However, the upper value of the control parameters should be limited depending on the design standard of controller bandwidths [30]. In addition, improving the control structure or adopting more advanced controllers may be better measures for LFO suppression.

5.3. Scope of Future Work

It has been demonstrated in Section 3.3 that the negative resistance caused by the DVC is the root reason for LFOs. Tuning of control parameters can mitigate LFO, but the selected range of parameters is limited by the requirements for dynamic performance. Naturally, it is expected from the control perspective that the impact of LFO can be mitigated by modifying the DC-link voltage controller, such as adopting H_∞ control [31]. However, this may lead to new problems such as the selection of the weighting function, so more detailed studies are required in the future. Moreover, it is worth trying to adopt other advanced control strategies, such as passivity-based control, fuzzy-based control, predictive control, etc, to improve the stability of the train-network system.

On the other hand, the reference frame of the impedance model in the d-q frame is synchronized with the operating trajectory of the fundamental frequency, so frequency coupling components from the coordinate transformation are ignored during the modeling process, which may affect the modeling accuracy. Based on the linear time-periodic theory, the harmonic state space (HSS) model containing multiple cross-coupling dynamics and harmonic components may be helpful in providing accurate assessments of LFO issues in the train-network system. In addition, the analysis results have been verified in the HIL experimental platform due to hardware limitations, but it is still necessary to conduct more realistic experimental verification in the physical platform in the future.

6. Conclusions

This paper proposes a quantitative stability assessment method that achieves mechanism analysis of formation and impact factors for the LFO in the train-network system. As the conventional case-based methods rely

on case analysis results without clear quantitative justifications, a system stability margin indicator is defined and derived for quantitative assessment by combining the improved Nyquist criterion and simplified system impedance model. Theoretical analysis based on the explicit expression of the stability margin indicator reveals that the negative resistance induced by the DC-link voltage controller in the impedance model leads to the risk of a negative stability margin indicator, thereby causing LFO. The parameter tuning can affect system stability by simultaneously affecting the frequency at IZP and the real part of the dominant eigenvalue, which is demonstrated by clear mathematical derivation considering two typical parameters as cases, the number of trains and the proportional gain of DVC. Since the theoretical quantification method improves the interpretability of analysis results compared to the conventional case-based method, it can be applied to the impedance-based stability analysis of various power electronic converter systems.

Appendix A. Expressions of Matrices in Impedance Model

The matrices in the small signal impedance model of the single-phase converter under TDCC in Section II-B are shown as follows. In addition to the variables already defined in Table I, ω_o is the fundamental rotational angular frequency, s is the Laplace operator, I_d^{ref} is the steady-state value of the d-axis reference current. U_d, U_q, I_d, I_q, D_d and D_q are the steady-state values of input current, input voltage, and duty ratio of converters in the d-q frame, which can be expressed as:

$$\begin{cases} U_d = U_o, U_q = 0 \\ I_d = (U_d - \sqrt{U_d^2 - (8R_n/R_d)U_{dc}^2}) \Big/ 2R_n, I_q = 0 \\ D_d = 2U_d/(I_d R_d), D_q = (-\omega_o L_n I_d)/U_{dc} \end{cases}$$

$$\mathbf{M}_{UI} = \begin{bmatrix} sL_n + R_n & -\omega_o L_n \\ \omega_o L_n & sL_n + R_n \end{bmatrix} + \frac{R_d}{2(1 + sC_d R_d)} \begin{bmatrix} D_d^2 & D_d D_q \\ D_d D_q & D_q^2 \end{bmatrix}$$

$$\mathbf{M}_{IU} = (\mathbf{M}_{UI})^{-1}$$

$$\mathbf{M}_{UD} = \begin{bmatrix} U_{dc} & 0 \\ 0 & U_{dc} \end{bmatrix} + \frac{R_d}{2(1 + sC_d R_d)} \begin{bmatrix} D_d I_d & D_d I_q \\ I_d D_q & D_q I_q \end{bmatrix}$$

$$\mathbf{M}_{ID} = -\mathbf{M}_{IU}\mathbf{M}_{UD}$$

$$\mathbf{M}_{DEL} = \begin{bmatrix} 1/(1+sT_d) & 0 \\ 0 & 1/(1+sT_d) \end{bmatrix}$$

$$\mathbf{M}_{CC} = \begin{bmatrix} K_{pCC}/U_{dc} & 0 \\ 0 & K_{pCC}/U_{dc} \end{bmatrix}$$

$$\mathbf{M}_{COM} = \begin{bmatrix} -(R_n/U_{dc}) & 0 \\ -(\omega_o L_n/U_{dc}) & 0 \end{bmatrix}$$

$$\mathbf{M}_{DVC} = \begin{bmatrix} -(K_{pVC} + \dfrac{K_{iVC}}{s}) + \dfrac{(2\sqrt{2}U_{dc})}{U_o R_d} & 0 \\ 0 & 0 \end{bmatrix}$$

$$\mathbf{M}_{DCD} = \frac{R_d}{2(1+sC_dR_d)} \begin{bmatrix} I_d & I_q \\ 0 & 0 \end{bmatrix}$$

$$\mathbf{M}_{DCI} = \frac{R_d}{2(1+sC_dR_d)} \begin{bmatrix} D_d & D_q \\ 0 & 0 \end{bmatrix}$$

$$\mathbf{M}_{DC} = \begin{bmatrix} D_d/U_{dc} & 0 \\ D_q/U_{dc} & 0 \end{bmatrix}$$

$$\mathbf{M}_{EP} = \begin{bmatrix} \dfrac{1}{U_{dc}} & \dfrac{\omega_o L_n I_d^{ref} G_{PLL}}{U_{dc}} \\ 0 & \dfrac{1-(R_n+K_{pCC})I_d^{ref}G_{PLL}}{U_{dc}} \end{bmatrix}$$

$$\mathbf{M}_{BPF} = \begin{bmatrix} H_{dd} & H_{dq} \\ H_{qd} & H_{qq} \end{bmatrix}$$

$$\begin{cases} H = \dfrac{s\omega_o K_{BPF}}{s^2 + s\omega_o K_{BPF} + \omega_o^2} \\ H_{dd} = H_{qq} = \dfrac{1}{2}H(s+j\omega_o) + \dfrac{1}{2}H(s-j\omega_o) \\ H_{dq} = -H_{qd} = \dfrac{j}{2}H(s+j\omega_o) - \dfrac{j}{2}H(s-j\omega_o) \end{cases}$$

References

[1] H. Hu, Y. Shao, L. Tang, J. Ma, Z. He, S. Gao, Overview of harmonic and resonance in railway electrification systems, IEEE Trans. Ind. Applicat. 54 (5) (2018) 5227–5245. doi:10.1109/TIA.2018.2813967.

[2] G. Shangguan, X. Li, Review of stability analysis of high-speed rail traction power supply system, Int. Conf. Smart Grid Smart Cities, ICSGSC (2023) 166–171doi:10.1109/ICSGSC59580.2023.10319205.

[3] X. Lv, X. Wang, Y. Che, R. Fu, Eigenvalue-based harmonic instability analysis of electrical railway vehicle-network system, IEEE Trans. Transp. Electrific. 5 (3) (2019) 727–744. doi:10.1109/TTE.2019.2929406.

[4] H. Wang, W. Mingli, J. Sun, Analysis of low-frequency oscillation in electric railways based on small-signal modeling of vehicle-grid system in dq frame, IEEE Trans. Power Electron. 30 (9) (2015) 5318–5330. doi:10.1109/TPEL.2015.2388796.

[5] S. Wu, Z. Liu, Low-frequency stability analysis of vehicle-grid system with active power filter based on dq-frame impedance, IEEE Trans. Power Electron. 36 (8) (2021) 9027–9040. doi:10.1109/TPEL.2021.3049145.

[6] P. Frutos, J. M. Guerrero, I. Muniategui, I. Vicente, A. Endemano, F. Briz, Low-frequency oscillations analysis in ac railway networks using eigenmode identification (2021) 1573–1579doi:10.1109/ECCE47101.2021.9595947.

[7] H. Hu, H. Tao, F. Blaabjerg, X. Wang, Z. He, S. Gao, Train–network interactions and stability evaluation in high-speed railways–part i: Phenomena and modeling, IEEE Trans. Power Electron. 33 (6) (2018) 4627–4642. doi:10.1109/TPEL.2017.2781880.

[8] X. Wang, F. Blaabjerg, Harmonic stability in power electronic-based power systems: Concept, modeling, and analysis, IEEE Trans. Smart Grid. 10 (3) (2019) 2858–2870. doi:10.1109/TSG.2018.2812712.

[9] X. Meng, Z. Liu, Y. Liu, H. Zhou, I. A. Tasiu, B. Lu, J. Gou, J. Liu, Conversion and siso equivalence of impedance model of single-phase converter in electric multiple units, IEEE Trans. Transp. Electrific. 9 (1) (2023) 1363–1378. doi:10.1109/TTE.2022.3203006.

[10] Y. Liao, Z. Liu, H. Zhang, B. Wen, Low-frequency stability analysis of single-phase system with *dq*-frame impedance approach—part ii: Stability and frequency analysis, IEEE Trans. Ind. Applicat. 54 (5) (2018) 5012–5024. doi:10.1109/TIA.2018.2828386.

[11] Y. Liao, Z. Liu, H. Zhang, B. Wen, Low-frequency stability analysis of single-phase system with dq-frame impedance approach—part i: Impedance modeling and verification, IEEE Trans. Ind. Applicat. 54 (5) (2018) 4999–5011. doi:10.1109/TIA.2018.2832027.

[12] B. He, W. Chen, C. Zhang, Y. Yuan, C. Zhang, Impedance specifications for stability design of grid-connected dc distribution power systems, IEEE Trans. Ind. Electron. 71 (6) (2024) 5830–5843. doi:10.1109/TIE.2023.3294583.

[13] H. Hu, H. Tao, X. Wang, F. Blaabjerg, Z. He, S. Gao, Train–network interactions and stability evaluation in high-speed railways—part ii: Influential factors and verifications, IEEE Trans. Power Electron. 33 (6) (2018) 4643–4659. doi:10.1109/TPEL.2017.2781879.

[14] Y. Hong, Z. Shuai, H. Cheng, C. Tu, Y. Li, Z. J. Shen, Stability analysis of low-frequency oscillation in train-network system using rlc circuit model, IEEE Trans. Transp. Electrific. 5 (2) (2019) 502–514. doi:10.1109/TTE.2019.2905983.

[15] M. Chang, X. Wang, X. Lv, R. Kong, Modeling and low-frequency oscillation analysis of an asymmetrical traction power system connected to power grid, IEEE Trans. Transp. Electrific. 9 (1) (2023) 1750–1764. doi:10.1109/TTE.2022.3200994.

[16] H. Tao, H. Hu, X. Zhu, K. Lei, Z. He, A multifrequency model of electric locomotive for high-frequency instability assessment, IEEE Trans. Transp. Electrific. 6 (1) (2020) 241–256. doi:10.1109/TTE.2019.2960886.

[17] X. Meng, Z. Liu, G. Li, X. Chen, S. Wu, K. Hu, A multi-frequency input-admittance model of locomotive rectifier considering pwm sideband harmonic coupling in electrical railways, IEEE Trans. Transp. Electrific. 8 (3) (2022) 3848–3858. doi:10.1109/TTE.2022.3141445.

[18] B. Guo, X. Zhang, H. Ma, Y. Yang, X. Wang, Q. Tian, S. Jin, A series impedance reshaping control method considering pll dynamics for

grid-connected inverters under weak grid conditions, IEEE Trans. Ind. Electron. 71 (5) (2024) 4896–4910. doi:10.1109/TIE.2023.3279578.

[19] X. Xiong, B. Luo, L. Li, Z. Sun, F. Blaabjerg, Impedance reshaping method of dfig system based on compensating rotor current dynamic to eliminate pll influence, IEEE Transactions on Power Electronics 39 (4) (2024) 4006–4016. doi:10.1109/TPEL.2023.3346042.

[20] Y. Zhou, H. Hu, X. Yang, Z. Meng, Z. He, Impacts of quadrature signal generation-based plls on low-frequency oscillation in an electric railway system, IEEE Trans. Transp. Electrific. 7 (4) (2021) 3124–3136. doi:10.1109/TTE.2021.3086231.

[21] X. Jiang, H. Hu, X. Yang, Z. He, Q. Qian, P. Tricoli, Analysis and adaptive mitigation scheme of low-frequency oscillations in ac railway traction power systems, IEEE Trans. Transp. Electrific. 5 (3) (2019) 715–726. doi:10.1109/TTE.2019.2927128.

[22] P. Dey, S. Myint, P. Kirawanich, A. Saha, C. Sumpavakup, Fine tuning of on-board traction converters for high-speed electric multiple units at depot, IEEE Access 12 (2024) 22479–22489. doi:10.1109/ACCESS.2024.3362242.

[23] Y. Zhou, H. Hu, X. Yang, J. Yang, Z. He, S. Gao, Low frequency oscillation traceability and suppression in railway electrification systems, IEEE Trans. Ind. Applicat. 55 (6) (2019) 7699–7711. doi:10.1109/TIA.2019.2935194.

[24] H. Hu, Y. Zhou, X. Li, K. Lei, Low-frequency oscillation in electric railway depot: A comprehensive review, IEEE Trans. Power Electron. 36 (1) (2021) 295–314. doi:10.1109/TPEL.2020.2998702.

[25] C. Lin, H. Wang, Q. Deng, X. Ge, D. Liu, D. Xie, Y. Zuo, Impact analysis of digital delay on power factor and compensation strategy for electric traction pwm rectifier, IEEE Journal of Emerging and Selected Topics in Power Electronics 11 (1) (2023) 952–961. doi:10.1109/JESTPE.2022.3208931.

[26] C. Zhang, X. Wang, F. Blaabjerg, Analysis of phase-locked loop influence on the stability of single-phase grid-connected inverter,

in: 2015 IEEE 6th International Symposium on Power Electronics for Distributed Generation Systems (PEDG), 2015, pp. 1–8. doi:10.1109/PEDG.2015.7223089.

[27] R. Kong, X. Lv, X. Wang, Low-frequency oscillation analysis of train-network system with different types of trains connected, in: Proc. IEEE Conf. Ind. Electron. Appl. ICIEA, 2021, pp. 1530–1535. doi:10.1109/ICIEA51954.2021.9516148.

[28] A. Rygg, M. Molinas, C. Zhang, X. Cai, A modified sequence-domain impedance definition and its equivalence to the dq-domain impedance definition for the stability analysis of ac power electronic systems, IEEE J. Emerg. Sel. Top. Power Electron. 4 (4) (2016) 1383–1396. doi:10.1109/JESTPE.2016.2588733.

[29] R. Roy, T. Kailath, Esprit-estimation of signal parameters via rotational invariance techniques, IEEE Transactions on Acoustics, Speech, and Signal Processing 37 (7) (1989) 984–995. doi:10.1109/29.32276.

[30] D. Zhou, Y. Song, F. Blaabjerg, Chapter 5 - modeling and control of three-phase ac/dc converter including phase-locked loop, in: F. Blaabjerg (Ed.), Control of Power Electronic Converters and Systems, Academic Press, 2018, pp. 117–151. doi:https://doi.org/10.1016/B978-0-12-805245-7.00005-6.

[31] I. A. Tasiu, Z. Liu, S. Wu, W. Yu, M. Al-Barashi, J. O. Ojo, Review of recent control strategies for the traction converters in high-speed train, IEEE Trans. Transp. Electrific. 8 (2) (2022) 2311–2333. doi:10.1109/TTE.2022.3140470.